Editors' Suggestion

Subnanometer Control of the Heteroepitaxial Growth of Multimicrometer-Thick Ge/(Si,Ge) Quantum Cascade Structures

Enrico Talamas Simola,[1,*,‡] Michele Montanari,[1,‡] Cedric Corley-Wiciak,[2] Luciana Di Gaspare,[1] Luca Persichetti,[3] Marvin H. Zöllner,[2] Markus A. Schubert,[2] Tommaso Venanzi,[4] Marina Cagnon Trouche,[4] Michele Ortolani,[4] Francesco Mattioli,[5] Gianfranco Sfuncia,[6] Giuseppe Nicotra,[6] Giovanni Capellini,[1,2] Michele Virgilio,[7] and Monica De Seta[1,†]

[1] *Dipartimento di Scienze, Università degli Studi Roma Tre, Viale G. Marconi 446, Roma 00146, Italy*
[2] *IHP-Leibniz Institut für innovative Mikroelektronik, Im Technologiepark 25, Frankfurt (Oder) 15236, Germany*
[3] *Dipartimento di Fisica, Università di Roma "Tor Vergata", Via Della Ricerca Scientifica 1, Roma 00133, Italy*
[4] *Dipartimento di Fisica, Università di Roma "Sapienza", Piazzale A. Moro 2, Roma 00185, Italy*
[5] *IFN-CNR, via Cineto Romano 42, Rome 00156, Italy*
[6] *Istituto per la Microelettronica e Microsistemi (CNR-IMM), VIII Strada 5, Catania 95121, Italy*
[7] *Dipartimento di Fisica "E. Fermi", Università di Pisa, Largo Pontecorvo 3, Pisa 56127, Italy*

(Received 15 September 2022; revised 2 November 2022; accepted 28 November 2022; published 4 January 2023)

The fabrication of complex low-dimensional quantum devices requires the control of the heteroepitaxial growth at the subnanometer scale. This is particularly challenging when the total thickness of stacked layers of device-active material becomes extremely large and exceeds the multi-μm limit, as in the case of quantum cascade structures. Here, we use the ultrahigh-vacuum chemical vapor deposition technique for the growth of multi-μm-thick stacks of high Ge content strain-balanced Ge/SiGe tunneling heterostructures on Si substrates, designed to serve as the active material in a THz quantum cascade laser. By combining thorough structural investigation with THz spectroscopy absorption experiments and numerical simulations we show that the optimized deposition process can produce state-of-the-art threading dislocation density, ultrasharp interfaces, control of dopant atom position at the nanoscale, and reproducibility within 1% of the layer thickness and composition within the whole multilayer. We show that by using ultrahigh-vacuum chemical vapor deposition one achieves simultaneously a control of the epitaxy down to the sub-nm scale typical of the molecular beam epitaxy, and the high growth rate and technological relevance of chemical vapor deposition. Thus, this technique is a key enabler for the deposition of integrated THz devices and other complex quantum structures based on the Ge/SiGe material system.

DOI: 10.1103/PhysRevApplied.19.014011

I. INTRODUCTION

Nowadays, the field of semiconductor science is seeing an ever-growing intertwining between fundamental research and applications, shortening the bridge between discoveries in academic laboratories and the creation of devices. A clear example is the exploitation of quantum effects in nanoscale devices to improve performances and add functionalities while reducing their size. In particular, there is a steady interest for group-IV heterostructures driven by their peculiar electrical and optical properties and by their compatibility with the Si-based CMOS manufacturing, inspiring a plethora of innovative, potentially low-cost devices and systems [1]. Recently the focus has been primarily on high Ge content SiGe/Ge heterostructures, due to their various applications ranging from photonics [2] to quantum computing [3] and microelectronics [4]. However, their deposition on Si(001) presents several technological challenges, mainly due to the large mismatch of lattice parameters and thermal expansion coefficients between the Ge-rich structures and the substrate [5,6], that need to be addressed for an extensive use of this material system. Indeed, as witnessed by the large use of III-V compounds in high complex heterostructures and low-dimensional systems, the complete control over the heteroepitaxial process is one of the fundamental keys to enable a material platform [7]. Theoretical calculations

*enrico.talamassimola@uniroma3.it
†monica.deseta@uniroma3.it
‡These authors contributed equally to this work.

recently reported in Ref. [8,9] indicate that a suitable design of *n*-type Ge/SiGe quantum cascade laser (QCL) structures could lead to a net optical gain even at room temperature, with no Reststrahlen-band limitations, thus potentially overcoming the limitations of the commercial QCL devices based on III-V compound semiconductors, which are related to the strong electron-phonon coupling characteristic of these polar lattice materials [10]. The realization of such a Si-based device would have a significant impact on the long-sought quest to develop compact, low-cost, and powerful sources operating at room temperature in the entire far-infrared range of the electromagnetic spectrum. On the other hand, a THz QCL represents the ultimate challenge for a heteroepitaxial deposition process requiring the growth of several μm-thick, strain-compensated active regions, comprising hundreds of quantum wells (QWs) coupled by ultrathin tunneling barriers (approximately 1 nm). Albeit the demonstration of THz electroluminescence from this material system in Ref. [11] is a clear indication of the progress made in the field, several issues have still to be properly solved to achieve a working QCL. The band engineering of the electronic states of QCL devices requires subnanometric control over the Si and Ge composition profile, limited interface roughness and Si-Ge interdiffusion, and accurate localization of dopants. The latter task is complicated in the *n*-type Ge/SiGe material system by the well-known tendency of donor atoms to "float" on Ge during the growth [12]. All these features must be maintained during the growth of the whole QCL active region. On such thicknesses, the large lattice mismatch and different coefficients of thermal expansion of Ge-rich layers with respect to the Si substrate introduce the need for careful management of elastic and thermal in-plane strain. In this paper, we address the main technological issues mentioned above, discussing growth pathways and recipes for the deposition of multi-μm-thick strained Ge/SiGe multilayers on Si substrates, aiming at the realization of an active material for a QCL operating in the THz spectral region. To this aim, we report on the growth by ultrahigh-vacuum chemical vapor deposition (UHV CVD) of high-quality *n*-type Ge/SiGe QCL active regions deposited on a suitably designed SiGe/Ge/Si(001) reverse step-graded virtual substrate (RSG VS). The deposition process has been optimized to achieve a threading dislocation density (TDD) in the low 10^6 cm^{-2} scale. The samples have been suitably designed to account for the contributions of heteroepitaxial and thermal deformation in the active region whose impact on the crystalline quality and mechanical stability of the multilayered structure is investigated. In addition, the influence of both heteroepitaxial and thermal strain on the electronic states of the QCL structure is theoretically evaluated using a multivalley effective mass Schrödinger-Poisson solver. QCL active layers and VSs are structurally investigated by a combination of scanning transmission electron microscopy (STEM) and high-resolution x-ray diffraction (XRD). This structural information is complemented by the assessment of the TDD obtained using the etch-pit method and by the characterization of the surface morphology brought by atomic force microscopy (AFM). Furthermore, we carry out Fourier transform infrared spectroscopy (FTIR) in the THz range, to highlight relevant intersubband transitions (ISBTs) of the investigated QCL structures at zero bias. The comparison of experimental ISB absorption features with the results of Schrödinger-Poisson calculations granted valuable insight into the complex electronic subband structure and allowed an evaluation of the degree of control achieved on the doping profile and of the effective doping density in the active region.

II. EXPERIMENTAL DETAILS

Samples are grown by UHV CVD in a cold-wall reactor (base pressure approximately 1×10^{-10} Torr) using ultrapure germane and silane without carrier gases. The reacting gas pressure is optimized in the 1.2–1.5 mTorr range. The substrate, a 20×10 mm^2 Si(001) chiplet, is directly heated by a dc current flow. The active layer stack is deposited on top of a SiGe RSG VS [the Ge content is decreased by approximately 5% every 150 nm after the growth of a plastically relaxed Ge layer on the Si(001) substrate] [13–16] whose final Ge content is in the 90–97% range.

The typical QCL active region features compressively strained Ge wells alternated with ultrathin tensile-strained SiGe barriers with Ge contents x spanning the 77%–85% range, depending on the specific design. The growth temperature T_G of the active stack is 470 °C. Typical growth rates at 1.2 mTorr are 6.5 nm/min for the Ge well and 4.5 nm/min for the $Si_{0.20}Ge_{0.80}$ barrier. *n*-type doping is obtained by phosphine co-deposition over a thickness of 3 nm in a single Ge well per period. After the phosphine co-deposition the sample surface is exposed to H_2 to limit the P diffusion [12]. The growth of the single quantum cascade (QC) module is periodically repeated 50 times (20 times in samples characterized by THz absorption spectroscopy), for an overall thickness of about 5 μm. We point out that the deposition of such a thick heterostructure takes dozens of hours of process time, requiring the deposition system to be in stable conditions throughout the whole procedure. Notice that a cold-wall UHV CVD reactor, such as the one employed, does not require the interruption of the growth for chamber cleaning, a procedure that may have critical consequences on the quality of the deposition of such complex and thick structures.

The structural characterization of the samples is performed by STEM using a JEOL JEM-ARM200F scanning transmission electron microscope equipped with a cold-field emission gun (0.27 eV energy spread) and a probe aberration corrector (0.7 Å probe size). Images are

acquired at 200 kV using a high angle dark field (HAADF) detector (*Z*-contrast imaging). Sample lamellae for electron microscopy are prepared using the standard lamella lift-out technique in a dual channel focused ion beam (Dual-FIB) microscope. XRD is performed at room temperature with a Rigaku SmartLab μ-HR tool featuring a 0.8-kW microfocus rotating copper anode and a high-resolution setup utilizing a Ge(400) × 2 channel-cut beam monochromator and a Ge(220) × 2 analyzer crystal. FTIR spectroscopy is carried out in a side-illuminated single-pass waveguide configuration with a Bruker Vertex 70v (Bruker, Billerica, Massachusetts, USA) equipped with a He-flow cryostat. To this aim, the entry and exit facets of the samples are cut at a 70° angle with respect to the growth plane and the top surface close to the QC stack is coated with a metal bilayer (Ti/Au 10 nm/80 nm) to enhance the TM component in the active region [17]. To filter out polarization independent spectral features not related to ISB transitions, transmission spectra with TE polarized fields are also acquired and used to evaluate the dichroic transmission spectra $T(\omega) = T_{\mathrm{TM}}(\omega)/T_{\mathrm{TE}}(\omega)$. From $T(\omega)$, the dimensionless absorption coefficient $\alpha_{2\mathrm{D}}(\omega)$ is calculated [18]. In the simulations, electron states and ISB absorption spectra are calculated self-consistently in a Schrödinger-Poisson iterative scheme using a multivalley effective-mass model with parabolic subband dispersion [19,20].

III. RESULTS AND DISCUSSION

A. Growth and structural properties

The first step for the deposition of any high-quality Ge/SiGe multilayered structure on Si substrates is the realization of a SiGe VS having an in-plane lattice parameter matching that imposed by the strain compensation condition of the active region, and featuring a low TDD, possibly in the 10^5–10^6 cm^{-2} range. As a matter of fact, TDs have the dual effect of worsening the crystalline quality and generating acceptorlike defect states, therefore, inducing an effective *p*-type doping background [21]. These drawbacks are particularly critical in a QCL due to the large thickness of the multilayered structure and to the fact that the TDD related *p*-type background is comparable in magnitude to the typical *n*-type doping used for the active layers of the QCL.

To achieve the appropriate lattice parameter for the strain compensation condition, the composition of the topmost relaxed SiGe layer in the VS should match the average composition of the active region $\bar{x} = (x_b t_b + x_w t_w)/(t_b + t_w)$, where x_b (x_w) is the Ge content of the barriers (wells), having a total thickness t_b (t_w). In an *n*-type QCL based on Ge/SiGe QWs, x_b has to be in the 0.75–0.85 range to achieve adequate electron confinement and subband energy spacing, while the electron tunnel between adjacent wells requires barrier thicknesses significantly smaller with respect to the well ones. Consequently, $\bar{x}$ usually ranges in the 0.90–0.97 interval.

Skibitzki *et al.* [22] have demonstrated that a drastic reduction in TDD can be achieved in Ge-rich $Si_{1-x}Ge_x$/Ge ($x \sim 0.95$) RSG VS deposited on Si by industry-grade RP CVD acting on the quality of the Ge layer alone, through the introduction of cyclic growth and annealing steps. We thus adopt and adapt this approach to our UHV CVD process, which in comparison features a growth rate approximately 5 times slower. We have prepared a series of samples with increasing Ge layer thickness, grown with a different number of annealing steps, each consisting of 10 min at 800 °C. On the Ge layer we deposit at 500°C a 1200-nm-thick $Si_{0.05}Ge_{0.95}$ layer. A sketch of the investigated samples and typical SEM images after Secco etching are reported in Fig. 1 where we also show a plot of the measured TDD as a function of the Ge-layer thickness. We observe a decrease of the TDD of more than one order of magnitude by increasing the Ge thickness from 700 to 2800 nm, reaching the very competitive value of 3×10^6 cm^{-2}. Increasing the Ge thickness beyond 5000 nm does not induce a further decrease of the TDD. The TDD values shown in Fig. 1 are, within the statistical error of the TDD measurements, in line with the state-of-the-art values reported in Ref. [22]. The similarity of the behavior observed in RP CVD and UHV CVD suggests that the growth rate does not play a major role in the TD annihilation, which mainly depends on the Ge layer thickness and on the total thermal budget dominated by the annealing steps.

Once the SiGe RSG VS (here after SiGe VS) is optimized, a second step towards a working QC structure is the accurate management of the strain in the active-layer superstructure. This task is further complicated by the difference in the thermal expansion coefficients of Si (2.6×10^{-6}/°C) and Ge (5.9×10^{-6}/°C). When the active region is strain compensated at the growth temperature T_G of 470 °C, it acquires a tensile thermal strain contribution ($\varepsilon_{\mathrm{th}} \sim 0.14\%$) upon cooling to room temperature, which becomes even larger at the cryogenic temperatures. This excess strain impacts on the properties of the QCL active stack in a twofold way. On one hand it might cause cracks, that could eventually lead even to an exfoliation of the epilayers [23], while on the other it may have a critical impact on the band-edge energy profile, given the large difference in the magnitude of the deformation potentials for the *L* and Δ valleys of the conduction band, whose energies are remarkably close in relaxed, Ge-rich, SiGe alloys [24]. In the *n*-type Ge/SiGe QCL structure, the lowest energy Δ states are confined in the tensile barriers (see Fig. 2) and their energy drops upon an increase in tensile strain, as it happens when cooling the device. In designing Ge/SiGe QCL structures, one must therefore carefully take into account the presence of Δ subbands, whose energy

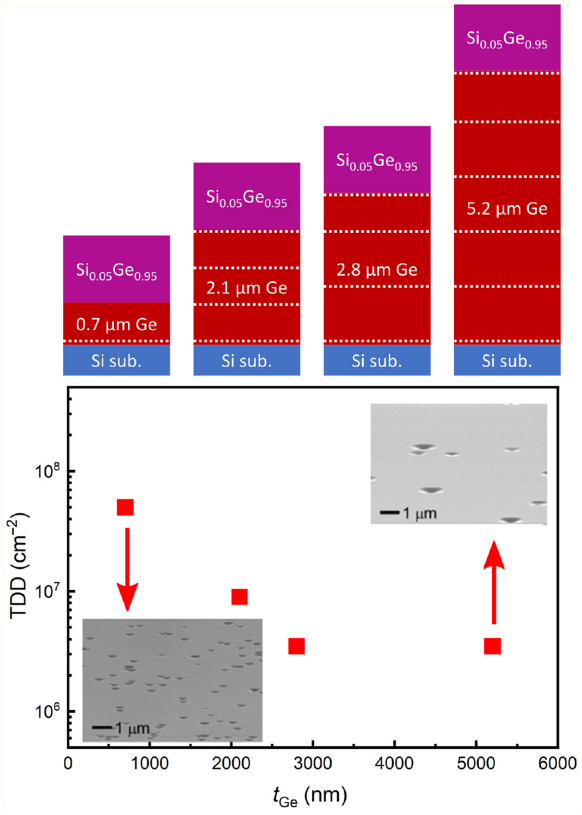

FIG. 1. TDD as a function of the Ge layer thickness. Etch pits are clearly visible in the SEM images of the samples after Secco etch. On top we report a sketch of the investigated structures where the annealing steps are reported with dotted lines.

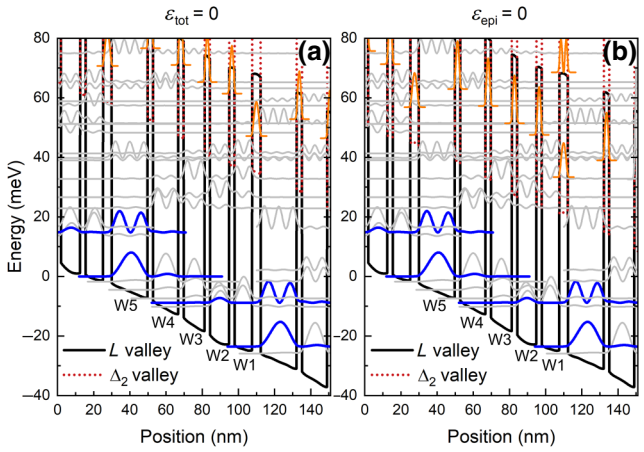

FIG. 2. QCL structures featuring $Si_{0.15}Ge_{0.85}$ barriers with $\bar{x} \sim 97\%$. Starting from the first quantum well W1 (reading from right to left), the nominal layer sequence with thicknesses in nanometers is 9.7/**3.0**/10.6/**3.0**/11.6/**3.0**/13.9/**3.0**/19.9/**4.7**. The Ge wells are in standard font, while the $Si_{0.15}Ge_{0.85}$ barriers are in bold. The black-solid and red-dotted lines refer to L and Δ band edges, respectively; the low energies L-superlattice subband in wells 1–4 are reported in gray, the laser levels in W5 in blue and the Δ states in orange. The QCL structure is calculated for $\varepsilon_{tot} = \varepsilon_{epi} + \varepsilon_{th} = 0$ (SCRT approach) (a) and $\varepsilon_{tot} = \varepsilon_{th} = 0.14\%$ (SCGT approach) (b).

must be high enough to suppress $L \leftrightarrow \Delta$ scattering events, which may critically complicate the transport of L-point carriers and thus suppress the optical gain. Such an effect can be mitigated either by decreasing the Si content in the SiGe barriers or by intentionally introducing a compressive epitaxial strain to compensate for the tensile thermal strain that appears upon lowering temperature.

To probe the impact of both epitaxial and thermal strain on the electronic structure and the crystalline quality of the samples, we investigate alternative strategies for the deposition of Ge/SiGe QC heterostructures, changing the Ge content in the SiGe VS in order to achieve a strain compensation of the active region at room temperature or at the growth temperature T_G:

1. *Strain compensation at room temperature (SCRT):* the SiGe VS has a Ge content lower than the average content in the active region so that the latter is grown under a compressive average epitaxial strain ε_{epi} equal in magnitude to the thermal tensile strain ε_{th} obtained upon cooling at room temperature after the deposition. In such conditions, the average total strain at room temperature $\varepsilon_{tot} = \varepsilon_{epi} + \varepsilon_{th}$ is zero. The compressive epitaxial strain pushes up the energy of the Δ states confined in the SiGe barriers, allowing a wider compositional range for the SiGe barriers, thereby increasing the design flexibility. However, given that the QW stack will not be strain compensated at T_G, the system may plastically relax by inducing the formation of misfit dislocations (MDs) and TDs in the active layers. Notice that in this approach room temperature could be substituted by any given "operating temperature" by tailoring the Ge content of the VS.

2. *Strain compensation at T_G* (SCGT): the SiGe VS has a Ge content equal to the average composition of the active layer, so to achieve strain compensation at T_G ($\varepsilon_{epi} \sim 0$). Consequently, the cooling of the sample from T_G down to the operating temperature induces an excess tensile thermal strain that has to be taken into account when designing the QCL band-energy profile. Furthermore, especially for thick active regions, the excess thermal strain at low T can impact the mechanical stability of the structure, which is prone to cracking.

In Fig. 2 we report the band-edge profile at room temperature under an applied bias of 3.7 kV/cm together with the relevant subband states, calculated for the QCL structure used in Ref. [11] to demonstrate ISB electroluminescence. This design comprises five Ge wells separated by $Si_{0.15}Ge_{0.85}$ tunneling barriers, and features an average Ge content $\bar{x} = 97\%$ and a total period thickness of 82.4 nm. The ISB laser transition is vertical, having both initial and

final states, portrayed as thick blue curves in Fig. 2, confined in well 5. The solid-black and dotted-red lines represent the L- and Δ-point band-edge profiles, respectively, while L states other than the ones involved in the lasing transition are reported in gray, and Δ states in orange. The QCL structure is calculated for $\varepsilon_{tot} = \varepsilon_{epi} + \varepsilon_{th} = 0$ [panel (a)] and $\varepsilon_{tot} = \varepsilon_{th} = 0.14\%$ [panel (b)]. In other words, Fig. 2(a) refers to the SCRT deposition strategy while Fig. 2(b) refers to the SCGT approach. As apparent from the comparison between (a) and (b), the Δ states at room temperature lie at lower energy in the SCGT case. Nevertheless, we point out that the design appears robust against the increase of tensile strain upon cooling, as the Δ states remain well above the relevant L-point subband. This is also true below room temperature, as evidenced by similar simulations run at 10 K, using the thermal expansion coefficients from Ref. [5]. We attribute this robustness to the relatively high Ge content used for the SiGe barriers. We note that, according to the simulations, by adopting the SCRT strategy the barrier Ge concentration can be lowered down to about 77% without the intrusion of Δ states in the energy range of the relevant L states.

To study the structural properties and crystalline quality of this kind of thick Ge/SiGe heterostructure, we grow a series of samples using the two above-mentioned strategies, repeating the QCL module $\times 50$, for a total active region thickness slightly below 5 μm. The SCRT and SCGT QCL structures are deposited on SiGe VSs having a TDD approximately 3×10^6 cm^{-2} and a final Ge content adequate for the respective strain compensation strategy.

Figures 3(a) and 3(b) show the XRD reciprocal space maps (RSMs) of the asymmetric 224 reflections of two QCL samples deposited using the SCRT and SCGT designs, respectively, and measured at room temperature.

The analysis of XRD data assesses that the SiGe VSs of the SCRT and SCGT samples have a Ge content of 90.0% and 95.9%, resulting in active regions having radically different strain states at room temperature: while the SCRT has a negligible measured average biaxial strain of $\varepsilon = 0.01\%$ the SCGT sample is under a tensile biaxial strain of $\varepsilon = 0.12\%$. The period thicknesses are 81.8 and 83.1 nm, respectively, in agreement within less than 1 nm with the nominal one (82.4 nm). While the superlattice (SL) peaks of the SCGT sample are both extremely sharp

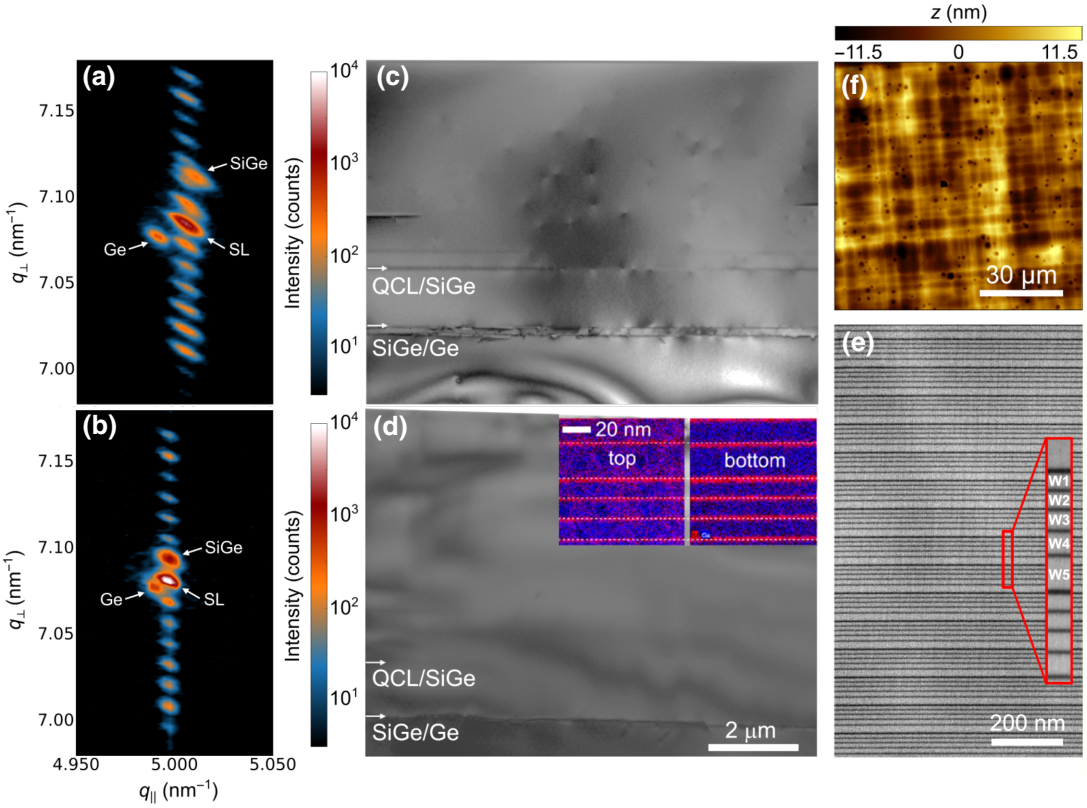

FIG. 3. (a),(b) XRD RSMs of asymmetric 224 reflections and (c),(d) TEM images of QCL samples deposited following the SCRT (a),(c) and the SCGT (b),(d) strategies. The positions of the SiGe/Ge interface in the VS and of the interface between the QCL stack and the SiGe VS are indicated by an arrow in (c),(d). In the inset of (d) we report the Ge and Si signals from scanning transmission electron microscopy with energy dispersive x-ray analysis (STEM EDX) acquired on the top and on the bottom of a 50-period QCL SCTG structure. In the panel on the right, we report (e) the STEM image of the first approximately 1.2 μm of the active region of a QCL SCGT structure and (f) the surface morphology measured by AFM (the scan area is 90×90 μm^2, and the z range is 22 nm).

and isotropic, those of the SCRT sample feature diagonal stripes along $\omega - \theta$, resulting in a significantly larger average FWHM in this direction (4.0 ± 0.1 arcprimes versus the 2.2 ± 0.1 of SCGT) and suggesting the presence of a nonuniform local tilt across the sample, which could develop as a result of a pile up of dislocations [23] promoted by the increased epitaxial strain. In contrast, the average FWHM of the SL peaks along the 2θ direction is comparable for the two samples, with values of 2.1 ± 0.1 and 1.9 ± 0.2 arcprimes, respectively.

TEM images of the SCRT and SCGT samples are reported in Figs. 3(c) and 3(d), respectively. For the SCRT design, we observe a significant presence of MDs at the QCL/SiGe VS interface and within the QCL stack, attributed to the plastic relaxation of the latter through a modified Frank-Read multiplication mechanism [25] driven by the compressive strain it experiences at T_G. Our data demonstrate that for samples having a several μms thick active region, the SCGT strategy is mandatory to achieve the best crystalline quality of the multilayer structures. As a matter of fact, the TEM image of the SCGT sample highlights the absence of MDs associated with plastic relaxation in the active region, confirming the effectiveness of strain compensation during the growth. Furthermore, the EDX images acquired at the bottom and on the top of the structure and shown in the inset of Fig. 3(d) indicate high reproducibility of the structure throughout the whole active region (period variations are $<1\%$, i.e., at the sub-nm level), in agreement with the sharp SL peaks present in the XRD RSM of the same sample.

Figure 3(e) shows a STEM image acquired on the deepest 15 periods of the SCGT sample, paired with a magnified detail of two consecutive periods. The existence of sharp interfaces (within the resolution of the STEM EDX tool) throughout the whole sample indicates that possible annealing effects, occurring during the growth once the interface is buried, do not induce a significant intermixing at the T_G of 470 °C. Note that atom probe tomography measurements recently obtained from $20\times$ $Ge/Si_{0.2}Ge_{0.8}$ asymmetric coupled quantum wells grown in the same conditions indicate interface widths of 1.1 nm and rms interface roughness of 0.18 nm independently of the depth in the stack of the analyzed interface [26]. We point out that the measured interface width in our samples is at least 2.5 times narrower than those reported in the literature for SiGe/Ge heterostructures of similar compositions but deposited with different techniques [27,28]. In particular, we find that the most striking difference existing between Ge/SiGe multilayer samples grown by UHV CVD as in our case and by RP CVD is the sizably higher heterointerface width and the asymmetry of the Ge on SiGe and SiGe on Ge heterointerfaces observed in the latter case [28]. The AFM image of the SCGT sample reported in Fig. 3(f) demonstrates that the surface is smooth with a rms roughness R_q of few nms ($R_q = 1.6$ nm as calculated from a $25 \times 25\ \mu m^2$ scan). Furthermore, we do not observe the presence of cracks or bending. This can be favored by the small size of the samples ($20 \times 10\ mm^2$) and/or the simultaneous growth, occurring in our reactor geometry, of the same epitaxial layers on both the top and bottom surface of the substrate (a sketch of the sample holder and the XRD data acquired on the back surface are reported in Figs. S1–S3 within the Supplemental Material [29]) with the epitaxial stack on the back surface of the substrate acting as a back stressor, which may hinder the bending and cracking of the samples [30].

B. THz intersubband absorption

To gain further insight on the degree of control achieved by the growth process, we investigate the THz intersubband features of the TM-polarized absorption spectra by means of FTIR spectroscopy performed at various lattice temperatures. The samples consist of 20 repetitions of the SCGT design previously described, and differ for the *n*-type donor spatial profile, which is achieved by means of phosphine co-deposition ($N_d \sim 3 \times 10^{17}\ cm^{-3}$): the dopants are deposited in the central 3 nm of either well 2 (SW2 sample) or 4 (SW4 sample).

The *L*-band edge profiles, energy levels, and square moduli of the electron wave functions at 10 K, calculated for SW2 and SW4, are reported in Figs. 4(a) and 4(b), respectively. The dotted line represents the Fermi level. The corresponding TM absorption spectra, simulated at different lattice temperatures *T*, are reported in Fig. 4(c) for direct comparison with the measured ones [Fig. 4(d)].

Our simulations indicate that in the absence of vertical bias, the band bending, which is controlled by the adopted doping profile, determines the activation of selected ISBTs thereby affecting the spectral shape of the TM absorption, especially at low temperature. This would not hold true in a biased QCL since the electrostatic potential due to the charge unbalance between ionized donors and electronic carriers (Hartree potential) would be significantly smaller than the voltage drop on each period, therefore having a limited influence on the subband energy ordering. In our undoped, unbiased design, however, the subbands related to the fundamental QW states in the W4, and W5 wells have very similar energies; hence at low *T* the band bending associated with the Hartree potential is strong enough to shuffle those energies, ultimately controlling the relative populations in the initial state. Indeed, the simulations predict that in SW2, the electronic carriers tend to occupy mainly the W5 fundamental subband because of the low confinement energy associated to this large well, while only a residual fraction of carrier sits in the W2 fundamental level. It follows that a single dominant absorption peak, due to vertical transitions in W5, is expected at approximately 15 meV (red arrows), with a minor feature at approximately 37 meV (orange arrow) being related to

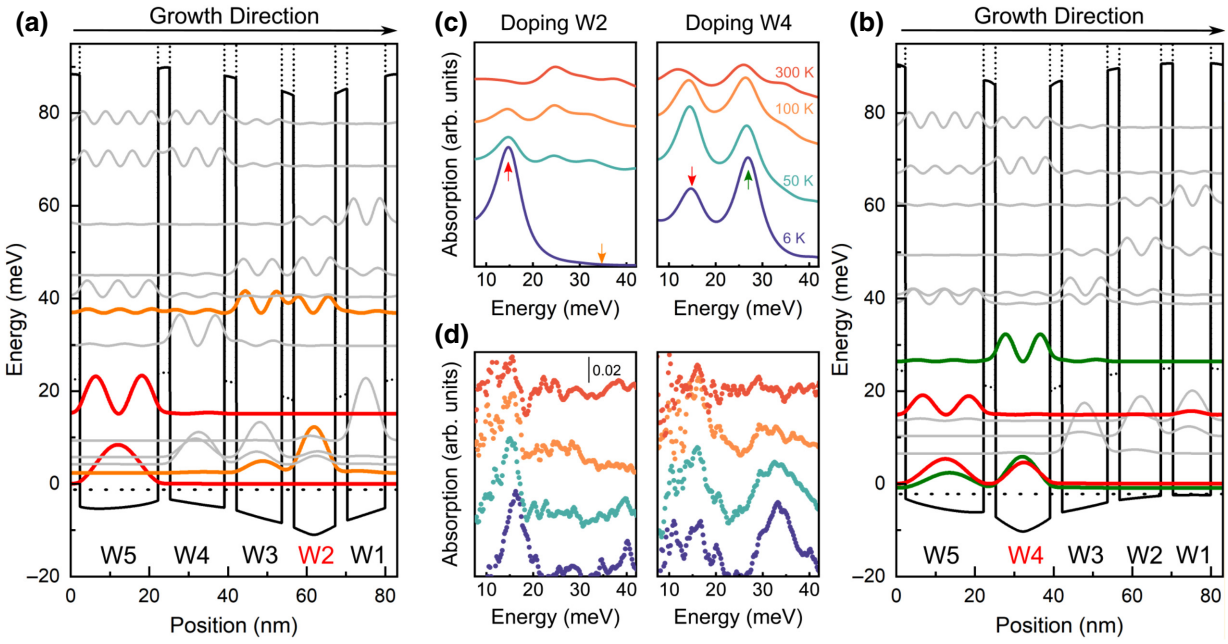

FIG. 4. *L*-band profile, energy levels and square modulus of the electron wave functions of SW2 (a) and SW4 (b) at 10 K. Temperature-dependent simulated and measured absorption spectra of both samples are reported in (c),(d), respectively.

ISB absorption in W2. On the other hand, when donor ions are located in the W4 well, the downward energy shift due to the electrostatic effect also activates a higher energy (approximately 27 meV, green arrow) vertical transition in W4, in addition of the vertical transition in W5. Upon increasing the lattice temperature, the energy differences among the fundamental QW subbands caused by the spatial donor profile become comparable with the thermal excitation energy, and thus we predict similar spectra shapes for SW2 and SW4.

The experimental spectra of the two samples, acquired at different temperatures and reported in Fig. 4(d), are in good agreement with the simulations. The dichroic absorption spectrum of SW2, measured at 6 K, features a single absorption peak at 15 meV having a full width at half maximum $\Gamma = 4$ meV. Interestingly, both the peak position and its width are in good agreement with the features of the ISB emission peak observed in the electroluminescence measurements of Ref. [11], performed with QCL samples having the same design. Furthermore, as predicted by the simulations, upon increasing the lattice temperature we experimentally observe a transfer of spectral weight towards higher energy, thermally activated, ISBT transitions. As for SW4, the spectrum acquired at 6 K exhibits a peak at about 15 meV related to the ISBT in W5 alongside a second, more intense absorption feature at 32 meV related to the ISBT in W4, in quite good agreement with our numerical predictions. The slight difference between the predicted and experimental W4 transition energy (5 meV) can be attributed to uncertainties in the precise values of the SiGe material parameters used in the numerical code such as the electron effective mass and the barrier and well band offset affecting the higher-energy states to a greater extent. Notice that in SW4 the lower-energy peak is characterized by a larger width ($\Gamma = 7$ meV) with respect to the one measured in SW2. We attribute this finding to the larger impact of the ionized impurity scattering on the ISB dephasing time [31], caused by the greater proximity of donor ions to the spatial region where the W5 wave functions involved in the transition are confined. The differences observed in the low-T absorption spectra of the two samples assess the accuracy of the UHV CVD technique in controlling the phosphorus profile, since they are entirely ascribable to the spatial distribution of the dopants. We notice that, owing to the low dopant concentration and the small doped thickness used here, this information is difficult to retrieve by standard techniques such as secondary ion-mass spectroscopy.

The electron sheet density per period n_{2D}, as estimated from the area defined by the ISB absorption resonance curve, [18] is approximately 3×10^{10} cm^{-2} for both samples. This value is in good agreement with the nominal one if taking into account the expected p-type background related to the presence of TDs. In samples with a TDD in the 10^6 cm^{-2} range, as in our case, a p-type background density of about 5×10^{15} cm^{-3} is estimated [21]. With a period length L_{per} approximately 100 nm for the QCL module investigated here, these density values give rise to an effective hole sheet density per period of about 5×10^{10} cm^{-2}, a value similar to the difference observed between the effective n_{2D} value estimated by FTIR and the nominal

doping. As a final remark, the good agreement observed between the predicted and measured absorption energies and oscillator strengths of the ISBTs can be regarded as an independent evidence of the high degree of accuracy achieved in the growth of complex multilayered heterostructures.

IV. CONCLUSIONS

In this work, we demonstrate the effectiveness of UHV CVD for the deposition of strain-balanced Ge/SiGe multilayer stack, comprising hundreds of quantum wells, coupled by ultrathin tunneling barriers. The improvement of the crystal quality in the high Ge content range (approximately 95%) of the SiGe virtual substrate, obtained by increasing the Ge buffer layer thickness and introducing annealing steps at 800 °C, allows us to obtain a very low TDD (3×10^6 cm^{-2}), thus suppressing this scattering source and its detrimental contribution to the carrier transport and to the effective doping density profile. To further optimize the strain compensated active region, we accurately investigate how both the heteroepitaxial and thermal strain impact on the electronic and mechanical properties. Indeed, the large mismatch between the lattice thermal expansion coefficient of Si and Ge induces a tensile deformation when the structure is cooled down after the growth, possibly causing bowing and cracking. We find that the simultaneous growth of the epilayer films on both sides of the Si substrate, enabled by the peculiar substrate heating solution adopted here, favors the mechanical stability of the heterostructure. Furthermore, we show thanks to numerical simulations that even small distortions of the lattice, as those due to the thermal strain, can critically affect the subband levels' alignment and consequently the target tunneling transport rates. We demonstrate that this is related to the presence of parasitic states, usually confined in the SiGe barriers and associated to Δ-band edges, whose energy downshifts for increasing tensile strain. Our numerical data highlights the relevance of properly accounting for the temperature dependence of the strain field, especially when designing devices that operate at temperatures much lower than the growth temperature. Finally, leveraging on the role of band-bending effects in MQW THZ structures caused by the charge unbalance, we discuss an experimental procedure to probe the doping concentration along the growth direction. By combining THz FTIR spectroscopy and numerical simulations, we are able to observe the influence of the spatial distribution of donors with an accuracy greater than that usually obtained by SIMS measurements. This technique allowed us to assess the nanometric control of the dopant distribution achieved by using the UHV CVD technique.

In conclusion, upon relying on the thorough structural characterization and on the agreement between THz ISBT absorption data and simulations, we demonstrate sub-nm/nm control over SiGe composition profile, interface roughness, interdiffusion, and localization of dopants in several μm-thick tunneling multilayer structures. These results represent a significant step forward in the SiGe epitaxy and in the use of this material platform for the development of integrated photonic quantum devices.

ACKNOWLEDGMENTS

This work is supported by Regione Lazio, Program POR FESR 2014-2020, Project No. A0375-2020-36579 "Teralaser" and by the European Union's Horizon 2020 research and innovation program under Grant Agreement No. 766719 (FLASH).

[1] K. Wada and L. C. Kimerling, *Photonics and Electronics with Germanium* (Wiley, Weinheim, 2015).

[2] I. A. Fischer, M. Brehm, M. De Seta, G. Isella, D. J. Paul, M. Virgilio, and G. Capellini, On-chip infrared photonics with Si-Ge-heterostructures: What is next?, APL Photonics **7**, 050901 (2022).

[3] G. Scappucci, C. Kloeffel, F. A. Zwanenburg, D. Loss, M. Myronov, J.-J. Zhang, S. De Franceschi, G. Katsaros, and M. Veldhorst, The germanium quantum information route, Nat. Rev. Mater. **6**, 926 (2021).

[4] Y. Bogumilowicz, J. Hartmann, J. Damlencourt, B. Vandelle, A. Abbadie, A. Papon, G. Rolland, P. Holliger, C. Di Nardo, P. Besoon, T. Ernst, T. Billon, C. Auknette, N. Daval, O. Rayssac, B. Ghyselen, N. Cherkashin, A. Claverie, B. Cluzel, and V. Calvo, High Ge content Si/SiGe heterostructures for microelectronics and optoelectronics purposes, Proc.—Electrochem. Soc. 7, 665 (2004).

[5] G. Capellini, M. De Seta, P. Zaumseil, G. Kozlowski, and T. Schroeder, High temperature X ray diffraction measurements on Ge/Si(001) heterostructures: A study on the residual tensile strain, J. Appl. Phys. **111**, 073518 (2012).

[6] H. Ye and J. Yu, Germanium epitaxy on silicon, Sci. Technol. Adv. Mater. **15**, 024601 (2014).

[7] Z. Alferov, Heterostructures for optoelectronics: History and modern trends, Proc. IEEE **101**, 2176 (2013).

[8] D. Paul, The progress towards terahertz quantum cascade lasers on silicon substrates, Laser. Photonics Rev. **4**, 610 (2010).

[9] T. Grange, D. Stark, G. Scalari, J. Faist, L. Persichetti, L. Di Gaspare, M. De Seta, M. Ortolani, D. J. Paul, G. Capellini, S. Birner, and M. Virgilio, Room temperature operation of *n*-type Ge/SiGe terahertz quantum cascade lasers predicted by non-equilibrium Green's functions, Appl. Phys. Lett. **114**, 111102 (2019).

[10] M. S. Vitiello, G. Scalari, B. Williams, and P. D. Natale, Quantum cascade lasers: 20 years of challenges, Opt. Express **23**, 5167 (2015).

[11] D. Stark, M. Mirza, L. Persichetti, M. Montanari, S. Markmann, M. Beck, T. Grange, S. Birner, M. Virgilio, C. Ciano, M. Ortolani, C. Corley, G. Capellini, L. Di Gaspare, M.

De Seta, D. J. Paul, J. Faist, and G. Scalari, Thz intersubband electroluminescence from *n*-type Ge/SiGe quantum cascade structures, Appl. Phys. Lett. **118**, 101101 (2021).

[12] K. Ismail, J. O. Chu, K. L. Saenger, B. S. Meyerson, and W. Rausch, Modulation-doped *n*-type Si/SiGe with inverted interface, Appl. Phys. Lett. **65**, 1248 (1994).

[13] G. Capellini, M. De Seta, Y. Busby, M. Pea, F. Evangelisti, G. Nicotra, C. Spinella, M. Nardone, and C. Ferrari, Strain relaxation in high Ge content SiGe layers deposited on Si, J. Appl. Phys. **107**, 063504 (2010).

[14] M. Montanari, M. Virgilio, C. L. Manganelli, P. Zaumseil, M. H. Zoellner, Y. Hou, M. A. Schubert, L. Persichetti, L. Di Gaspare, M. De Seta, E. Vitiello, E. Bonera, F. Pezzoli, and G. Capellini, Photoluminescence study of interband transitions in few-layer, pseudomorphic, and strain-unbalanced Ge/GeSi multiple quantum wells, Phys. Rev. B **98**, 195310 (2018).

[15] M. Montanari, C. Ciano, L. Persichetti, C. Corley, L. Baldassarre, M. Ortolani, L. Di Gaspare, G. Capellini, D. Stark, G. Scalari, M. Virgilio, and M. De Seta, Thz intersubband absorption in *n*-type $Si_{1-x}Ge_x$ parabolic quantum wells, Appl. Phys. Lett. **118**, 163106 (2021).

[16] M. D. Seta, G. Capellini, M. Ortolani, M. Virgilio, G. Grosso, G. Nicotra, and P. Zaumseil, Narrow intersubband transitions in *n*-type Ge/SiGe multi-quantum wells: Control of the terahertz absorption energy trough the temperature dependent depolarization shift, Nanotechnology **23**, 465708 (2012).

[17] M. Helm, in *Intersubband Transition in Quantum Wells: Physics and Device Applications I*, Semiconductors and Semimetals, Vol. 62, edited by H. C. Liu and F. Capasso (Elsevier, Amsterdam, 1999), p. 1.

[18] Y. Busby, M. De Seta, G. Capellini, F. Evangelisti, M. Ortolani, M. Virgilio, G. Grosso, G. Pizzi, P. Calvani, S. Lupi, M. Nardone, G. Nicotra, and C. Spinella, Near- and far-infrared absorption and electronic structure of Ge-SiGe multiple quantum wells, Phys. Rev. B **82**, 205317 (2010).

[19] L. Bagolini, M. Montanari, L. Persichetti, L. Di Gaspare, G. Capellini, M. Ortolani, M. De Seta, and M. Virgilio, Disentangling elastic and inelastic scattering pathways in the intersubband electron dynamics of *n*-type Ge/SiGe quantum fountains, Phys. Rev. B **101**, 245302 (2020).

[20] C. Ciano, M. Virgilio, M. Montanari, L. Persichetti, L. Di Gaspare, M. Ortolani, L. Baldassarre, M. Zoellner, O. Skibitzki, G. Scalari, J. Faist, D. Paul, M. Scuderi, G. Nicotra, T. Grange, S. Birner, G. Capellini, and M. De Seta, Control of Electron-State Coupling in Asymmetric Ge/Si-Ge Quantum Wells, Phys. Rev. Appl. **11**, 014003 (2019).

[21] H. Tetzner, I. A. Fischer, O. Skibitzki, M. M. Mirza, C. L. Manganelli, G. Luongo, D. Spirito, D. J. Paul, M. De Seta, and G. Capellini, Current leakage mechanisms related to threading dislocations in Ge-rich SiGe heterostructures grown on Si(001), Appl. Phys. Lett. **119**, 153504 (2021).

[22] O. Skibitzki, M. H. Zoellner, F. Rovaris, M. A. Schubert, Y. Yamamoto, L. Persichetti, L. Di Gaspare, M. De Seta, R. Gatti, F. Montalenti, and G. Capellini, Reduction of threading dislocation density beyond the saturation limit by optimized reverse grading, Phys. Rev. Mater. **4**, 103403 (2020).

[23] S. Assali, S. Koelling, Z. Abboud, J. Nicolas, A. Attiaoui, and O. Moutanabbir, 500-period epitaxial $Ge/Si_{0.18}Ge_{0.82}$ multi-quantum wells on silicon, J. Appl. Phys. **132**, 175304 (2022).

[24] M. M. Rieger and P. Vogl, Electronic-band parameters in strained $Si_{1-x}Ge_x$ alloys on $Si_{1-y}Ge_y$ substrates, Phys. Rev. B **48**, 14276 (1993).

[25] J. Tersoff and F. K. LeGoues, Competing Relaxation Mechanisms in Strained Layers, Phys. Rev. Lett. **72**, 3570 (1994).

[26] T. Grange, S. Mukherjee, G. Capellini, M. Montanari, L. Persichetti, L. Di Gaspare, S. Birner, A. Attiaoui, O. Moutanabbir, M. Virgilio, and M. De Seta, Atomic-Scale Insights into Semiconductor Heterostructures: From Experimental Three-Dimensional Analysis of the Interface to a Generalized Theory of Interfacial Roughness Scattering, Phys. Rev. Appl. **13**, 044062 (2020).

[27] A. Bashir, K. Gallacher, R. W. Millar, D. J. Paul, A. Ballabio, J. Frigerio, G. Isella, D. Kriegner, M. Ortolani, J. Barthel, and I. MacLaren, Interfacial sharpness and intermixing in a Ge-SiGe multiple quantum well structure, J. Appl. Phys. **123**, 035703 (2018).

[28] Y. Yamamoto, O. Skibitzki, M. A. Schubert, M. Scuderi, F. Reichmann, M. H. Zöllner, M. D. Seta, G. Capellini, and B. Tillack, Ge/SiGe multiple quantum well fabrication by reduced-pressure chemical vapor deposition, Jpn. J. Appl. Phys. **59**, 10 (2020).

[29] See Supplemental Material at http://link.aps.org/supplemental/10.1103/PhysRevApplied.19.014011 for a comparison between the growth on the front-side of the sample and the "collateral" growth happening on the back side, by means of XRD analysis.

[30] P. Storck and M. Vorderwestner, Semiconductor wafer with a heteroepitaxial layer and a method for producing the wafer (U.S. Patent US20090236696A1, Sep. 2009).

[31] M. Virgilio, D. Sabbagh, M. Ortolani, L. Di Gaspare, G. Capellini, and M. De Seta, Physical mechanisms of intersubband-absorption linewidth broadening in *s*-Ge/SiGe quantum wells, Phys. Rev. B **90**, 155420 (2014).